Published for SISSA by Springer
Received: August 23, 2022
Accepted: October 13, 2022
Published: October 27, 2022

Search for sub-eV axion-like particles in a stimulated resonant photon-photon collider with two laser beams based on a novel method to discriminate pressure-independent components

The SAPPHIRES collaboration

Yuri Kirita,[a] **Takumi Hasada,**[a] **Masaki Hashida,**[b,c] **Yusuke Hirahara,**[a] **Kensuke Homma,**[a,1] **Shunsuke Inoue,**[b,d] **Fumiya Ishibashi,**[a] **Yoshihide Nakamiya,**[b,e] **Liviu Neagu,**[e,f] **Akihide Nobuhiro,**[a] **Takaya Ozaki,**[a] **Madalin-Mihai Rosu,**[e] **Shuji Sakabe**[b,d] **and Ovidiu Tesileanu**[e]

[a] *Graduate School of Advanced Science and Engineering, Hiroshima University, 1-3-2 Kagamiyama, Higashi-Hiroshima, Hiroshima 739-8526, Japan*
[b] *Institute for Chemical Research, Kyoto University, Gokasho, Uji, Kyoto 611-0011, Japan*
[c] *Research Institute of Science and Technology, Tokai University, 4-1-1 Kitakaname, Hiratsuka, Kanagawa 259-1292, Japan*
[d] *Graduate School of Science, Kyoto University, Kitashirakawa Oiwake-cho, Sakyo-ku, Kyoto 606-8502, Japan*
[e] *Extreme Light Infrastructure-Nuclear Physics (ELI-NP) and Horia Hulubei National Institute for R&D in Physics and Nuclear Engineering (IFIN-HH), 30 Reactorului St., P.O. Box MG-6, Bucharest-Magurele, Judetul Ilfov RO-077125, Romania*
[f] *National Institute for Laser, Plasma and Radiation Physics, 409 Atomistilor, P.O. Box MG-36, Magurele, Judetul Ilfov RO-077125, Romania*
E-mail: kirita@quark.hiroshima-u.ac.jp, hasada@quark.hiroshima-u.ac.jp, hashida.masaki.3z@kyoto-u.ac.jp, hirahara@quark.hiroshima-u.ac.jp, khomma@hiroshima-u.ac.jp, sinoue@laser.kuicr.kyoto-u.ac.jp, isibasi@quark.hiroshima-u.ac.jp, yoshihide.nakamiya@eli-np.ro, liviu.neagu@eli-np.ro, nobuhiro@quark.hiroshima-u.ac.jp, ozaki@quark.hiroshima-u.ac.jp, madalin.rosu@eli-np.ro, sakabe@laser.kuicr.kyoto-u.ac.jp, ovidiu.tesileanu@eli-np.ro

[1] Corresponding author.

https://doi.org/10.1007/JHEP10(2022)176

JHEP10(2022)176

Abstract: Sub-eV axion-like particles (ALPs) have been searched for by focusing two-color near-infrared pulse lasers into a vacuum along a common optical axis. Within the focused quasi-parallel collision system created by combining a creation field (2.5 mJ/47 fs Ti:Sapphire laser) and a background inducing field (1.5 mJ/9 ns Nd:YAG laser), the detection of signal photons via stimulated resonant photon-photon scattering by exchanging ALPs was attempted in a vacuum chamber. The signal wavelength can be determined via energy-momentum conservation in the vacuum, and it coincides with that determined from the atomic four-wave-mixing (aFWM) process. In this work, the pulse energies were one order of magnitude higher than those in the previous search, allowing aFWM from optical elements to be observed as a pressure-independent background for the first time, in addition to the residual-gas-originating aFWM following a quadratic pressure dependence. In principle the four-wave-mixing process in vacuum via ALP exchanges (vFWM) must also be pressure-independent, so the development of a new method for discriminating the optical-element aFWM is indispensable for increasing the pulse energies to the values needed for future upgraded searches. In this paper, we will present the established method for quantifying the yield from the optical-element aFWM process based on the beam cross-section dependence. With the new method, the number of signal photons was found to be consistent with zero. We then successfully obtained a new exclusion region in the relation between ALP-photon coupling, g/M, and the ALP mass m, reaching the most sensitive point $g/M = 1.14 \times 10^{-5}\,\mathrm{GeV}^{-1}$ at $m = 0.18\,\mathrm{eV}$.

Keywords: Dark Matter, Particle and Resonance Production, Other Experiments, Photon Production

ArXiv ePrint: 2208.09880

JHEP10(2022)176

Contents

JHEP10(2022)176

1 Introduction

Axion and axion-like particles (ALPs) can be generic candidates for the dark components of the Universe if their couplings to matter are reasonably weak with the proper masses. Axion is a pseudoscalar boson associated with the breaking of the Peccei-Quinn symmetry which is introduced to solve the strong CP problem [1], and could be cold dark matter. Additionally, a *miracle* scenario [2] which explains both dark matter and inflation predicts the existence of an ALP having a mass range that overlaps with the axion models. Scalar fields, such as dilaton [3, 4] and chameleon [5, 6], have been widely explored in attempts to explain the dark energy in the Universe.

In the low mass region, many experiments [7–10] have been conducted focusing on ALP-photon coupling as a method of searching for ALPs. In this paper, we focus on the coupling between sub-eV ALPs and two photons. For scalar (ϕ)- and pseudoscalar (σ)-type ALPs, the following effective Lagrangians are assumed:

$$-L_\phi = gM^{-1}\frac{1}{4}F_{\mu\nu}F^{\mu\nu}\phi, \quad -L_\sigma = gM^{-1}\frac{1}{4}F_{\mu\nu}\tilde{F}^{\mu\nu}\sigma, \tag{1.1}$$

where g is a dimensionless constant for a given energy scale M at which a relevant global symmetry is broken. $F^{\mu\nu} = \partial^\mu A^\nu - \partial^\nu A^\mu$ is the electromagnetic field strength tensor, and its dual tensor is defined[1] as $\tilde{F}^{\mu\nu} \equiv \frac{1}{2}\varepsilon^{\mu\nu\alpha\beta}F_{\alpha\beta}$ with the Levi-Civita symbol ε^{ijkl}.

[1]We explicitly note that the factor 1/2 is newly multiplied to the definition used in the previous search [11].

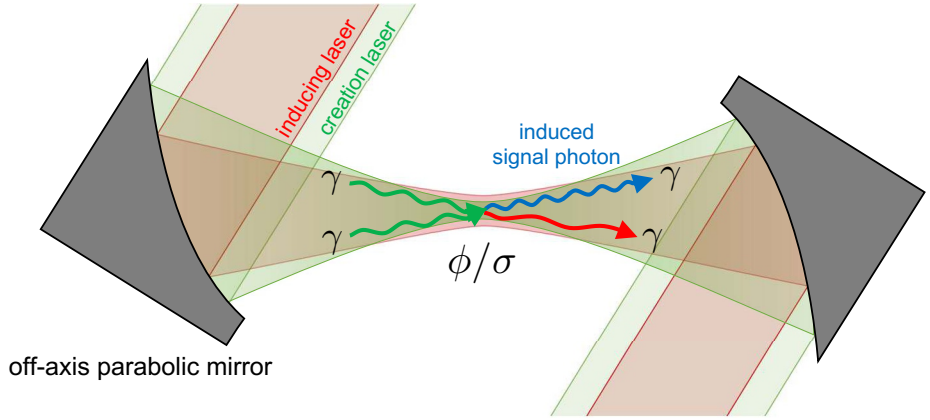

Figure 1. Concept of a stimulated resonant photon-photon collision (vFWM process) via scalar (ϕ) or pseudoscalar (σ) fields. The coaxially combined green and red lasers, which are, respectively, used to create ALPs and to simultaneously induce those decays, are focused with a parabolic mirror in a vacuum. The wavy arrows represent two-body photon-photon scattering via ALP exchange in the laser fields. The induced signal photons with wavelength determined by energy-momentum conservation (blue arrow) are produced primarily around the focal point.

The SAPPHIRES collaboration searches for sub-eV ALPs via stimulated resonant photon-photon collisions (SRPC) by focusing two lasers in the manner illustrated in figure 1. A collision between two photons with a shallow incident angle in a creation field (Ti:Sapphire laser, the green beam in figure 1) produces an ALP resonance state while a background field (Nd:YAG laser, the red beam in figure 1) simultaneously induces the ALP decay. The wavelength of the signal photon (the wavy blue line) in the final state can differ from those of the lasers due to energy-momentum conservation. In the terminology of laser physics, this process can be interpreted as four-wave-mixing in vacuum (vFWM).

Figure 2 illustrates possible background sources with respect to vFWM. The dominant background process is four-wave mixing originating from atoms (aFWM). Both vFWM and aFWM are kinematically similar and indistinguishable with the exception of polarization states of signal photons, which depend on the types of exchanged ALPs. The dominant background source of aFWM is residual gas around the focal spot in the vacuum chamber that interacts with the high-intensity [W/m^2] laser fields. However, a new background component originating from optical elements along the propagation path of the laser fields is expected to be significant for much higher intensities, even when the beams have not been focused. In addition to aFWM, other background sources include the plasma generated by focusing lasers and the thermal noise in the photo-detection device.

In the SAPPHIRES00 search [11], we looked for ALPs with sub-mJ-level pulse lasers. We provided a way to evaluate the background yields from residual-gas-originating aFWM, plasma, and other noise sources. In this work, we used a 2.5 mJ/47 fs Ti:Sapphire laser and a 1.5 mJ/9 ns Nd:YAG laser, whose energies are one order of magnitude higher than those in SAPPHIRES00. Since the yield from optical-element aFWM was observed for the first time with mJ-level laser pulses, we have established a new method for discriminating between the new background component and signals from vFWM. In the next section

JHEP10(2022)176

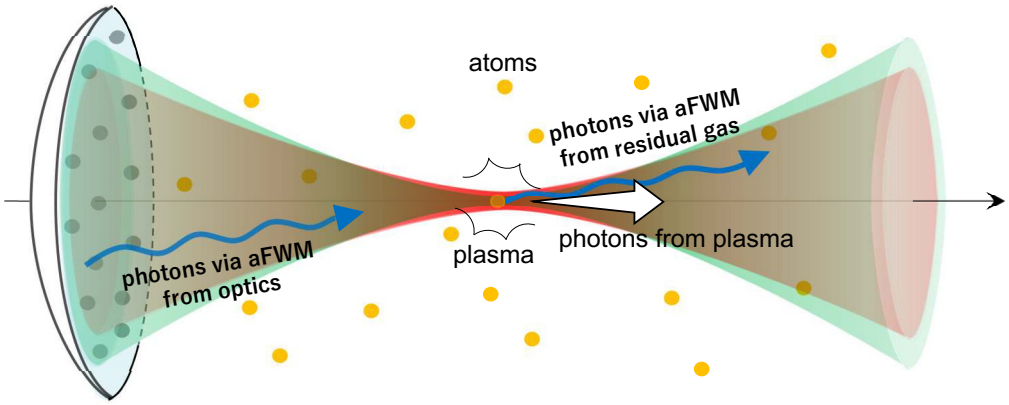

Figure 2. Possible background sources originating from atoms and plasma in the quasi-parallel collision system. The atomic four-wave mixing (aFWM) photons can be produced from residual gas and optical elements, with the same wavelength as the signal photons. Plasma can be generated by focusing high-intensity laser fields at the focal point and ionizing the residual gas around it.

we summarize the principles behind the new method, which is based on the beam cross-section dependence. We then present the new search results obtained using this method and provide new exclusion regions for the relation between ALP coupling with photons and ALP mass. Finally, we conclude with prospects for the future work.

2 Method for discriminating against optical-element atomic four-wave-mixing

To extract the yield from ALP exchanges, that is, vacuum-originating FWM n_{vFWM}, we first summarize the summation rules for the total number of signal-like FWM photons n_{FWM}:

$$n_{\mathrm{FWM}} \equiv n_{\mathrm{vFWM}} + n_{\mathrm{aFWM}} \tag{2.1}$$

with

$$n_{\mathrm{aFWM}} \equiv n_{\mathrm{gas}} + n_{\mathrm{opt}}, \tag{2.2}$$

where n_{gas} and n_{opt} are the numbers of photons from residual-gas-originating aFWM and optical-element aFWM, respectively. Another expression for n_{FWM} based on the observed numbers of signal-like photons, denoted with capital characters as $N_{\mathrm{S,C,I,P}}$, is given by

$$n_{\mathrm{FWM}} = N_{\mathrm{S}} - (N_{\mathrm{C}} - N_{\mathrm{P}}) - (N_{\mathrm{I}} - N_{\mathrm{P}}) - N_{\mathrm{P}} \tag{2.3}$$

with

$$N_{\mathrm{S}} = n_{\mathrm{FWM}} + n_{c\mathrm{PLS}} + n_{i\mathrm{PLS}} + n_{\mathrm{PED}} \tag{2.4}$$

$$N_{\mathrm{C}} = n_{c\mathrm{PLS}} + n_{\mathrm{PED}} \tag{2.5}$$

$$N_{\mathrm{I}} = n_{i\mathrm{PLS}} + n_{\mathrm{PED}} \tag{2.6}$$

$$N_{\mathrm{P}} = n_{\mathrm{PED}}, \tag{2.7}$$

JHEP10(2022)176

where S, C, I, and P denote combinations of laser beams (see figure 6 for details): S for a signal-expected case with both creation and inducing beams, C for a case with only a creation laser, I for a case with only an inducing laser, and P for a case without beams, hence, a pedestal of the detection system. $n_{c\mathrm{PLS}}$ and $n_{i\mathrm{PLS}}$ are the expected numbers of photons due to plasma formation with only creation and inducing beams, respectively.

As had already been performed in past searches [11–13], n_{FWM} in eq. (2.1) can be determined from eq. (2.3) based on measurements in the different beam combinations above. Past searches have also confirmed that n_{gas} follows a square dependence on the residual gas pressure. Thus, we first take a look at the pressure dependence of n_{FWM} by changing vacuum pressure values. If n_{FWM} exhibits pressure independence, then it implies that

$$n_{\mathrm{FWM}} = n_{\mathrm{vFWM}} + n_{\mathrm{opt}} \tag{2.8}$$

in a low-pressure environment because vFWM and optical-element aFWM are, in principle, pressure independent. Therefore, we need a method for evaluating n_{vFWM} by discriminating against n_{opt}.

The principle for discrimination is illustrated in figure 3. In any FWM process, n_{FWM} originates from the space-time overlapping region of the two laser pulses. Figure 3(a) shows cross sections of a creation laser (dotted and dashed lines) with different beam diameters and an inducing laser (solid line) with a fixed diameter measured at one of the optical elements before focusing the two laser beams. Figure 3(b) shows the corresponding cross sections at a focal plane after focusing. In figure 3(a), the peripheral ring beyond the inducing diameter (the area between the dotted and solid lines) will never be able to produce aFWM because the inducing field does not exit there. Therefore, when the creation beam diameter is beyond the range of the inducing beam diameter, as shown by the dotted line, optical-element aFWM yields must be constant even if the creation beam diameter is increased. On the other hand, in figure 3(b), since the beam waist w_0 in an ideal Gaussian beam at a focal plane is expressed as [14]

$$w_0 \equiv \frac{f\lambda}{\pi(d/2)} \tag{2.9}$$

with laser photon wavelength λ, focal length f, and beam diameter d, the dotted area is fully contained within the range of the inducing focal spot. Increasing the creation beam diameter introduces a higher photon density at the focal point, that is, a higher beam intensity in $\mathrm{W/m^2}$. Thus, both n_{vFWM} and n_{gas} are expected to be strongly dependent on the creation beam diameter. Therefore, observing how n_{FWM} increases when the creation beam diameter is increased, especially in the case where the creation beam diameter is larger than that of the inducing beam, enables discrimination against the optical-element aFWM. If n_{FWM} behaves in a pressure-independent fashion in a low-pressure environment, then we can test the dependence on beam cross sections to investigate whether the vFWM process is included or not on top of the constant behavior from optical-element aFWM. We must therefore know in advance how n_{vFWM} behaves as a function of the beam cross sections.

JHEP10(2022)176

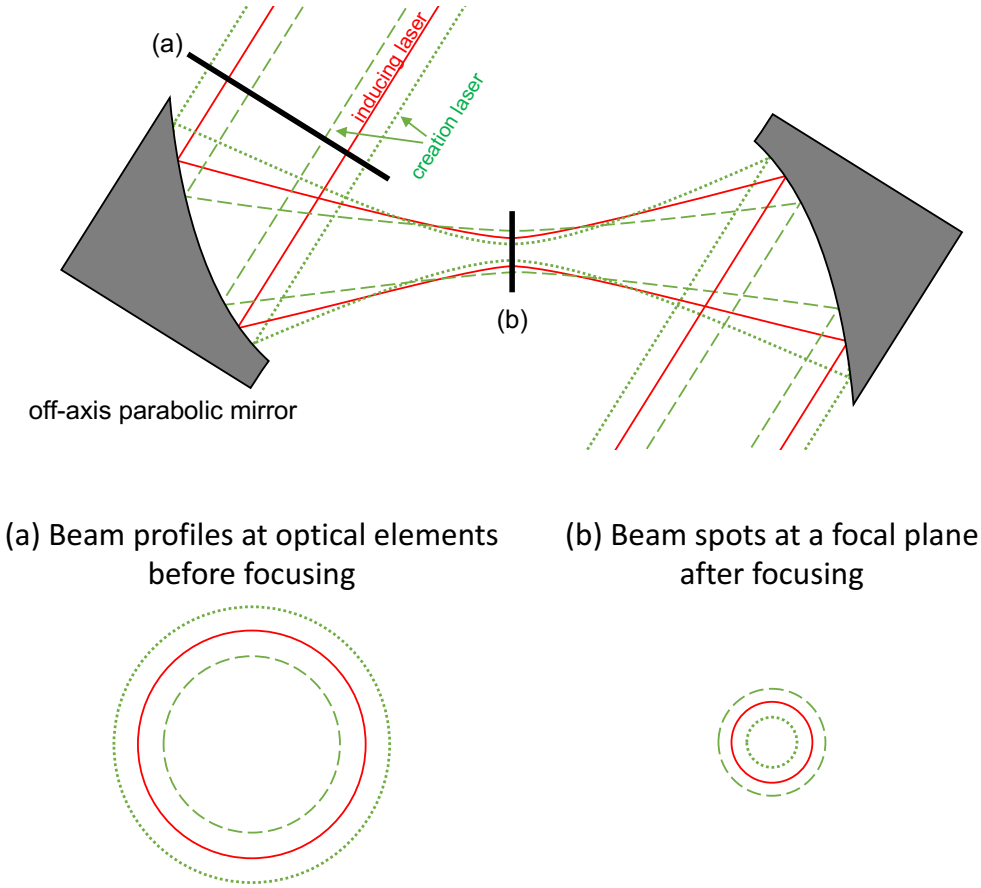

Figure 3. Relations between beam cross sections for creation and inducing lasers: (a) at planes in optical elements before focusing and (b) at the focal plane after focusing. (a) The creation and inducing laser cross sections are drawn with dotted and dashed green lines and a solid red line, respectively. The optical-element aFWM photons are produced at the overlapping areas between the cross sections of the creation and inducing beams. (b) Behavior of the two beams at a focal plane after focusing is illustrated. Since the beam waist is proportional to the inverse of the beam diameter at the focal point, a large (small) creation beam diameter makes the beam waist small (large) and the beam intensity higher (lower). Photons from vFWM and residual-gas-originating aFWM can be generated from the overlapping areas between the two beam cross sections, while optical-element aFWM photons are never produced.

The vFWM yield, which, more specifically from the particle physics point of view, is the signal yield per pulse collision from stimulated resonant photon-photon scattering, $\mathcal{Y}_{c+i}$, is factorized as [11, 15]

$$\mathcal{Y}_{c+i}[1] \equiv \frac{1}{4} N_c^2 N_i \mathcal{D}_{\rm I} \left[s/L^3 \right] \overline{\Sigma}_{\rm I} \left[L^3/s \right] . \tag{2.10}$$

N_c and N_i are the average number of photons in the two beams, with the subscripts c and i denoting the creation and inducing beams, respectively. $\mathcal{D}_{\rm I}$ is a space-time overlapping factor between the incident beams, and $\overline{\Sigma}_{\rm I}$ is the *interaction volume rate*, not the *interaction cross section* [11, 15], specified in the units within [ ], which are expressed in terms of length L and seconds s.

JHEP10(2022)176

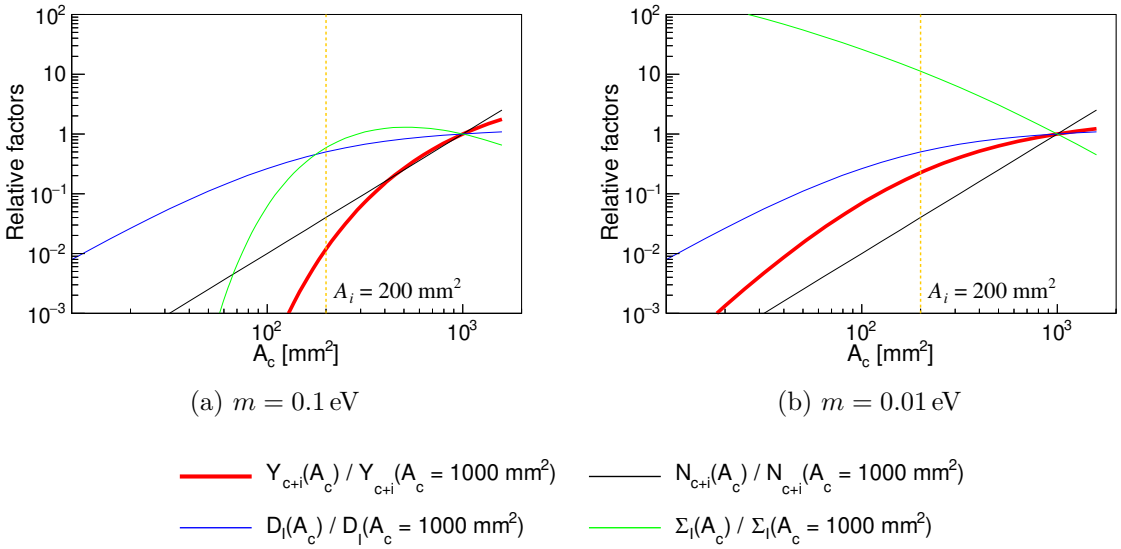

(a) $m = 0.1\,\mathrm{eV}$ (b) $m = 0.01\,\mathrm{eV}$

Figure 4. Behavior of individual factors in eq. (2.10) as a function of creation beam cross sections A_c with respect to a fixed inducing beam cross section $A_i = 200\,\mathrm{mm}^2$ (yellow dashed line) obtained by assuming an ALP mass of (a) $m = 0.1\,\mathrm{eV}$ and (b) $m = 0.01\,\mathrm{eV}$. The red, black, blue, and green curves indicate $\mathcal{Y}_{c+i}$, $\mathcal{N}_{c+i} \equiv \frac{1}{4}N_c^2 N_i$, $\mathcal{D}_\mathrm{I}$, and $\overline{\Sigma}_\mathrm{I}$, normalized by their values at $A_c = 1000\,\mathrm{mm}^2$, respectively. Since the creation beam cross section is cut by an iris (A1 in figure 5), the number of photons in a creation laser pulse N_c is proportional to A_c. $\overline{\Sigma}_\mathrm{I}$, which describes ALP-photon interactions, has the characteristic beam cross-section dependence, because ALP resonance masses depend on the incident angles of two stochastically selected photons from among those in the focused creation beam.

Figures 4(a) and 4(b) demonstrate how individual factors in eq. (2.10) behave as a function of the creation beam cross sections A_c with respect to a fixed inducing beam cross section $A_i = 200\,\mathrm{mm}^2$, represented by the yellow dashed line. The assumed ALP mass was $m = 0.1\,\mathrm{eV}$ and $m = 0.01\,\mathrm{eV}$, respectively. Individual factors are explained with different colors inside the figures and have individual normalizations of $A_c = 1000\,\mathrm{mm}^2$, which is close to the actual value of the maximum creation beam cross sections used in this work. What is important is the behavior of $\mathcal{Y}_{c+i}$ in the region $A_c > A_i$, shown with the red curves. Depending on the ALP mass, $\overline{\Sigma}_\mathrm{I}$ behaves differently, and the $\mathcal{Y}_{c+i}$ dependence on A_c obviously deviates from the constant behavior seen when optical-element aFWM contributes as the sole background source. Therefore, if $\mathcal{Y}_{c+i}$ exhibits a significant non-constant behavior for $A_c > A_i$ while in a low-pressure environment, then, in principle, we can determine the mass scale of ALPs from the creation beam cross-section dependence [15] in addition to testing the existence of ALPs.

3 Experimental setup

Figure 5 shows the experimental setup. It is almost identical to the setup used in the previous search [11]. For the creation and inducing fields we used a 47 fs-pulsed Ti:Sapphire laser, located at the Institute for Chemical Research in Kyoto University (T^6 system),

JHEP10(2022)176

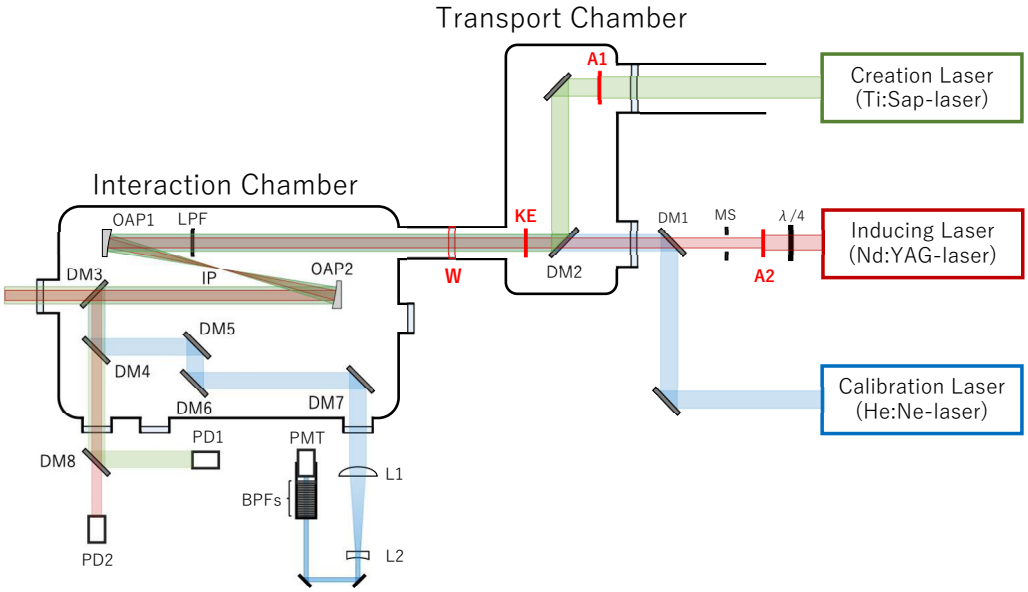

Figure 5. Experimental setup for this work. The basic design is the same as that in the previous search [11]. The propagations of individual lasers (creation laser, inducing laser, and calibration laser) are painted with green, red, and blue stripes, respectively. Ti:Sapphire and Nd:YAG lasers were used as the creation and inducing lasers. The calibration laser was a He:Ne laser, and it was used to obtain the acceptance of signal photons propagating from the Interaction point (IP) to the photomultiplier tube (PMT). The two irises (A1 and A2) were introduced in order to change the creation beam diameter and to fix the inducing beam diameter for the measurement of the beam cross-section dependence. Both beam diameters were determined using the knife-edge mechanism (KE). We intentionally introduced the window (W) not only to keep a low pressure value in the interaction chamber but also to enhance the background from optical-element aFWM, and to establish the method for discriminating against optical-element aFWM.

and a 9 ns-pulsed Nd:YAG laser. The central wavelengths of these lasers were 816 nm and 1064 nm, respectively. The signal central wavelength was expected to be 662 nm via FWM: $2\omega_c - \omega_i$ with creation photon energy ω_c and inducing photon energy ω_i. A linearly polarized (P-pol) creation beam and a circularly polarized (left-handed) inducing beam were combined at a beam combiner using a dichroic mirror (DM2) in the transport chamber, which was maintained at $\sim 10^{-2}$ Pa. The combined laser fields were focused coaxially into the interaction point (IP) in the interaction chamber, which was designed to reach $\sim 10^{-8}$ Pa but was operated at $\sim 10^{-5}$ Pa for this search. Since the pressure values in the two chambers were so different, we introduced a window (W) between them. To reduce the background amount in the upstream so that the photo-detection device could be operated without saturation, a set of long pass filters (LPF) for cutting the signal wavelength was inserted between the window and the focusing off-axis parabolic mirror (OAP1). A second off-axis parabolic mirror (OAP2), identical to OAP1, was placed at the symmetric position with respect to the IP to collect signal photons. The signal photon selection was made through a set of five identical dichroic mirrors (DM3 through DM7), and the collimated signal photons were detected by a photomultiplier tube (PMT) through a set of tight band-

JHEP10(2022)176

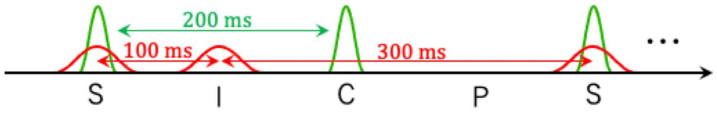

Figure 6. Four beam combinations with the two laser pulses. The green and red pulses are creation and inducing laser pulses, and the repetition rates are 5 Hz at equal and irregular intervals, respectively. We denote four pulse combinations: S for both laser pulses, C for only the creation laser pulses, I for only the inducing laser pulses, and P for a pedestal measure without laser pulses.

pass filters (BPFs) that rejected remnant beam photons. The voltage-time information was recorded with a waveform digitizer, and the peak finding algorithm was applied to obtain arrival times and the number of photons through amplitudes of waveforms. The detailed specifications for these devices and for the peak analysis method can be found in [11, 13]. To discuss the beam cross-section dependence of optical-element aFWM, we introduced two irises (A1 and A2) with circular apertures along the individual beam propagations: the c-Iris for changing the beam diameter of the creation laser and the i-Iris for fixing the beam diameter of the inducing laser. To accurately determine the beam diameters before focusing, the knife-edge mechanism (KE) was installed after the DM2.

4 Measurements

4.1 Arrival time distributions in four beam combinations

To evaluate n_{FWM} in eq. (2.3), we configured four beam combinations with the two laser pulses. The repetition rates of the creation and inducing laser pulses are 5 Hz at equal and irregular intervals, respectively, as illustrated in figure 6. We then measured the arrival time distributions of photon-like signals at the photomultiplier tube using peak finding on waveforms for four pulse combinations: two laser pulses (Signal pattern, S), only the creation laser pulses (Creation pattern, C), only the inducing laser pulses (Inducing pattern, I), and without laser pulses (Pedestal pattern, P). The expected sources of photons contained in individual patterns are summarized in table 1. The observed photons in the P pattern are pedestal components from all kinds of ambient noises, primarily from the thermal noise of the photo-detection device. The observed photons in the C and I patterns contain plasma-originating photons from the individual lasers and pedestals. The observed photons in the S pattern include signal photons and photons from all possible background sources.

Figure 7 shows the arrival-time distributions of observed photons in individual combinations of laser beams. The histograms for the S, C, I, and P patterns are shown in the upper left (Blue), upper right (Green), lower left (Purple) and lower right (Gray), respectively. The area between the two red lines represents the expected arrival time window for signal photons.

4.2 Pressure dependence of the number of FWM photons

Using subtractions between the four beam combinations based on eq. (2.3), we measured the number of FWM photons in the interaction chamber. It is known that the amount

JHEP10(2022)176

Four beam combinations	S pattern	C pattern	I pattern	P pattern
Characters	N_{S}	N_{C}	N_{I}	N_{P}
Vacuum FWM (n_{vFWM})	◯	—	—	—
Atomic FWM (n_{aFWM})	◯	—	—	—
Plasma in the creation laser ($n_{c\mathrm{PLS}}$)	◯	◯	—	—
Plasma in the inducing laser ($n_{i\mathrm{PLS}}$)	◯	—	◯	—
Noise (n_{PED})	◯	◯	◯	◯

Table 1. Sources of photons included in individual beam combination patterns. The characters $N_{\mathrm{S,C,I,P}}$ denote the numbers of observed photons in the individual combination patterns expressed by the subscripts.

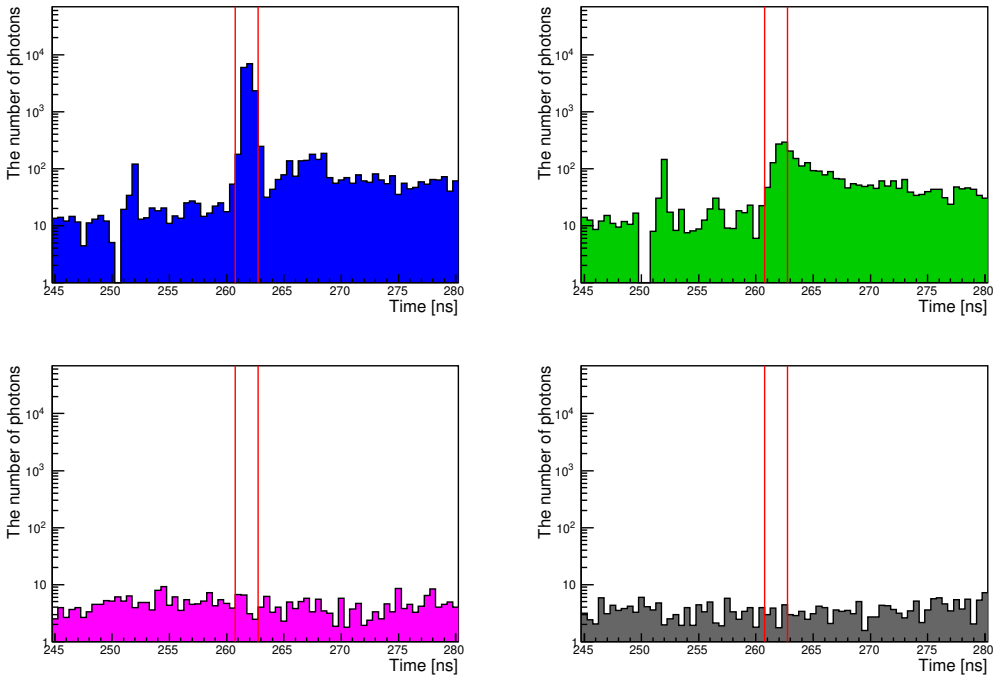

Figure 7. Arrival-time distributions of observed photons in individual beam combinations at 4.32×10^{-5} Pa. The red lines represent a time window within which signal photons are expected to arrive. The upper-left, upper-right, lower-left, and lower-right histograms correspond to the S, C, I, and P beam combinations, respectively.

of residual-gas-originating aFWM scales with the square of the pressure values [11–13]. Figure 8 shows the pressure dependence of the number of FWM photons per shot $\mathcal{N}$, fit with the function

$$\mathcal{N} = a + b\mathcal{P}^c, \tag{4.1}$$

where $\mathcal{P}$ is the pressure with fitting parameters a, b, and c. The fit result, $c = 2.05 \pm 0.09$, is consistent with the square scaling. From this result, we confirmed that the number of

JHEP10(2022)176

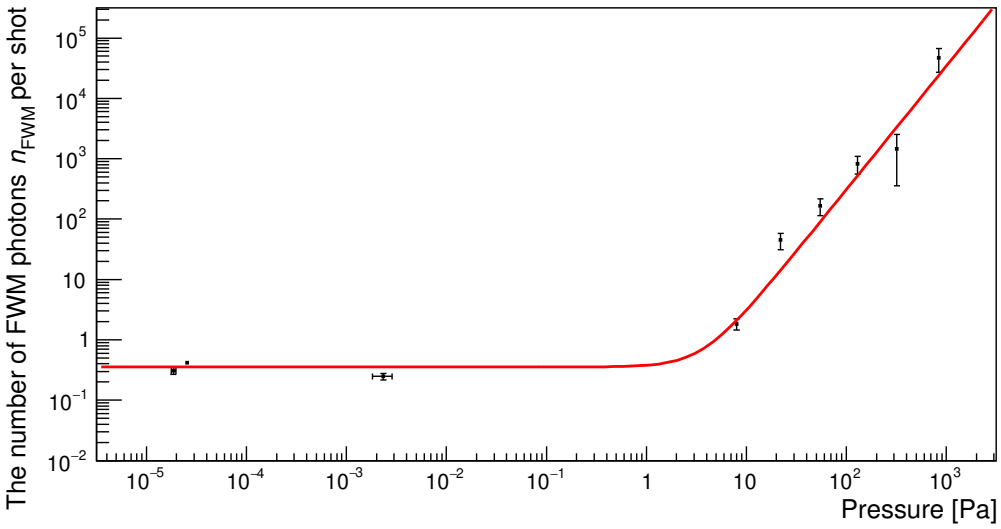

Figure 8. Pressure dependence of the number of observed FWM photons n_{FWM} per shot within the time window for expected signal arrival. The number of observed FWM photons follows the square of the pressure when the chamber is above 10 Pa. This means that residual-gas-originating FWM backgrounds are dominant in high pressure environments. Below 1 Pa, a nonzero constant component was observed for the first time.

FWM photons via the residual gas n_{gas} was negligibly small at 10^{-5} Pa. Additionally, the constant component was finally observed as $a = 0.35 \pm 0.02$ for the first time. More explicitly, figure 9 shows the arrival-time distribution after the subtraction between the four beam combinations, based on eq. (2.3) with total S-pattern statistics of 15,000 shots at 2.87×10^{-5} Pa. This pressure-independent component is considered to be a possible mixture of n_{vFWM} and n_{opt}, as introduced in eq. (2.8) of section 2.

4.3 Beam cross-section dependence of the number of observed photons

Figure 10 shows the beam cross-section dependence of the number of FWM photons at 10^{-5} Pa, where the beam cross sections of the creation laser A_c were changed with the variable size iris, c-Iris, while that of the inducing laser A_i was fixed at $A_i = 217\,\mathrm{mm}^2$ (yellow dashed line in figure 10). As discussed in section 2, we only need to consider the dependence on creation beam cross sections above the inducing beam cross section. We thus focused on the last four cross section points, and fitting was performed using the following linear function of the creation beam cross sections A_c (red line in figure 10):

$$\mathcal{N} = d + eA_c. \tag{4.2}$$

The slope e was obtained as $e = (-1.5 \pm 2.6) \times 10^{-4}$. Therefore, we conclude that the observed number of FWM photons is consistent with being constant as a function of the creation beam cross sections, indicating that the number of optical-element aFWM photons n_{opt} occupies the n_{FWM} in eq. (2.8).

JHEP10(2022)176

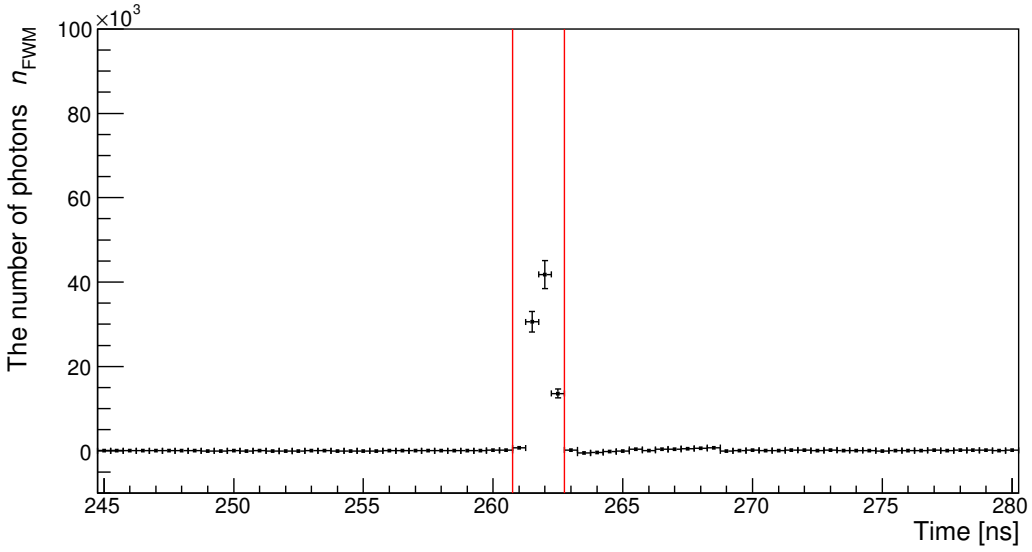

Figure 9. Arrival-time distribution of the number of observed photons after subtracting background photons from plasma and thermal noise, based on eq. (2.1) with total S-pattern statistics of 15,000 shots at 2.87×10^{-5} Pa. The region between the two red lines is the time window within which signal photons are expected to arrive.

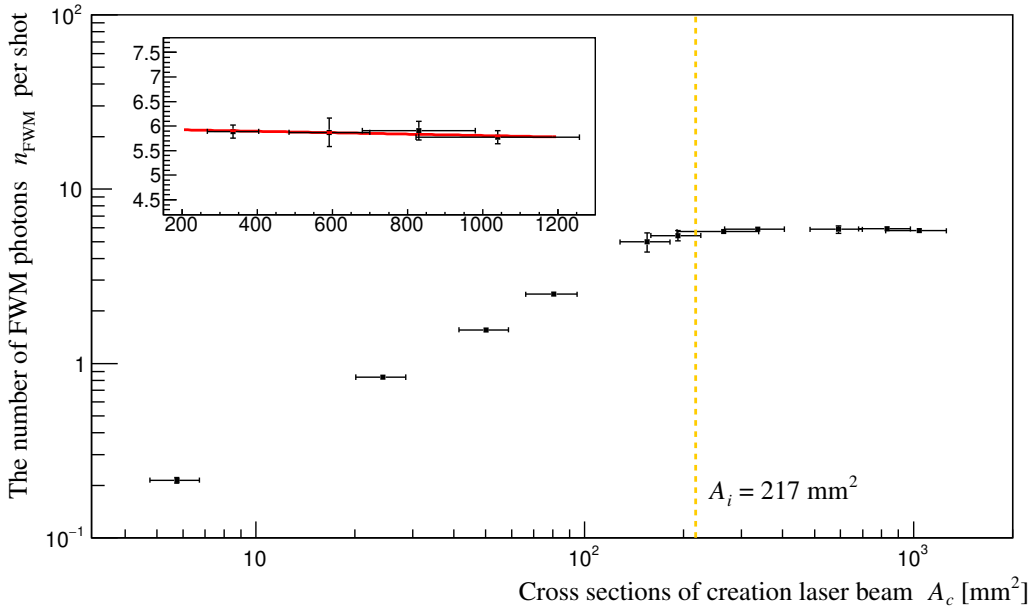

Figure 10. Creation beam cross-section dependence of the number of observed FWM photons n_{FWM} per shot, drawn on a double-logarithmic scale. The yellow dashed line is a fixed inducing pulse cross section $A_i = 217\,\mathrm{mm}^2$. Four datapoints from the right-most point, where creation pulse diameters are sufficiently larger than the inducing pulse diameter with considering errors, are shown enlarged in the insert with a linear scale. These were fitted with eq. (4.2), resulting in the slope $e = (-1.5 \pm 2.6) \times 10^{-4}$ represented by the red line. Since the number of observed FWM photons are independent of the creation pulse cross section in the $A_c > A_i$ region, the optical-element aFWM accounts for the observed photons.

JHEP10(2022)176

5 Exclusion regions in ALP coupling-mass relations

We obtained new exclusion regions in ALP coupling-mass relations by following the same procedure as in the previous publication [11]. With a set of laser beam parameters P, the number of ALP-originating signal photons, that is, vacuum-originating FWM n_{vFWM}, as a function of mass m and coupling g/M is expressed as

$$n_{\mathrm{vFWM}} = \mathcal{Y}_{c+i}(m, g/M; P) t_a r \epsilon, \tag{5.1}$$

where t_a is the data acquisition time, r is the repetition rate of the pulsed beams, and ϵ is the efficiency of detecting signal photons. For a set of m values and an n_{vFWM}, a set of coupling g/M is evaluated by solving this equation numerically. The laser parameters are summarized in table 2.

Since we conclude that the contribution from n_{vFWM} is consistent with null from the creation beam cross-section dependence, we can evaluate new exclusion regions in the coupling-mass relation based on the fact that the background distribution is only from the optical-element aFWM process. We do this by assuming the Gaussian distribution on n_{opt} because n_{opt} is obtained from subtractions between different trigger patterns whose baseline fluctuations are expected to individually follow Gaussian distributions. We focus on the result from the highest ALP mass range, which corresponds to n_{opt} at the maximum creation beam cross section, because a sensible mass m is expressed as $m = 2\omega_c \sin\vartheta$ with half the incident angles ϑ between two incident photons varying in the range $0 < \vartheta < \sin^{-1}(f/(d/2))$. A confidence level is thus defined with respect to the null hypothesis by stating that the observed n_{FWM} is all from the optical-element aFWM process.

A confidence level $1-\alpha$ for excluding the null hypothesis is expressed as

$$1 - \alpha = \frac{1}{\sqrt{2\pi}\sigma} \int_{\mu-\delta}^{\mu+\delta} e^{-(x-\mu)^2/(2\sigma^2)} dx = \mathrm{erf}\left(\frac{\delta}{\sqrt{2}\sigma}\right), \tag{5.2}$$

where μ is the expected value of an estimator x corresponding to n_{opt}, and σ is one standard deviation δn_{opt} on the measurement of n_{opt}. We assign the acceptance-uncorrected uncertainty for δn_{opt} from the quadratic sum of all error components in the following result by multiplying the total statistics of 15,000 shots in the S pattern:

$$n_{\mathrm{opt}} = (8.6613 \pm 0.0427\,(\mathrm{stat.}) \pm 0.0023\,(\mathrm{syst.I}) \pm 0.0009\,(\mathrm{syst.II})) \times 10^4 \,\mathrm{photons}. \tag{5.3}$$

Systematic error I originates from baseline fluctuations measured before the signal time window defined by the two red lines in figure 9, reflecting the possibility of different pedestal distributions depending on the different time domains. Systematic error II comes from the threshold value used to define the single photon waveform. We note that the uncertainty of the focal spot overlap factor evaluated in [11] is omitted in this analysis because the optical-element aFWM process is insensitive to it, due to the background only being produced when two parallel beams are propagating.

To obtain a confidence level of 95%, $2\alpha = 0.05$ with $\delta = 2.24\sigma$ was assigned, where a one-sided upper limit by excluding above $x + \delta$ [26, see eq. (36.56)] was applied. For the

JHEP10(2022)176

Parameter	Value
Creation pulse laser	
Centeral wavelength λ_c	816 nm
Relative linewidth, $\delta\omega_c/ < \omega_c >$	1.2×10^{-2}
Duration time of pulse, τ_c	40 fs
Measured pulse energy per τ_c, E_c	(2.53 ± 0.05) mJ
Pulse energy fraction within 3 σ_{xy} focal spot, f_c	0.78
Effective pulse energy per τ_c within 3 σ_{xy} focal spot	$E_c f_c = 1.97$ mJ
Effective number of creation photons, N_c	8.1×10^{15} photons
Beam diameter of pulse, d_c	$(36.4 \pm 2.2 \pm 3.1)$ mm
Polarization	linear (P-polarized state)
Inducing pulse laser	
Central wavelength, λ_i	1064 nm
Relative linewidth, $\delta\omega_i/ < \omega_i >$	1.0×10^{-4}
Duration time of pulse, $\tau_{i\text{beam}}$	9 ns
Measured pulse energy per $\tau_{i\text{beam}}$, E_i	(1.51 ± 0.02) mJ
Linewidth-based duration time of pulse, $\tau_i/2$	$\hbar/(2\delta\omega_i) = 2.8$ ps
Pulse energy fraction within 3 σ_{xy} focal spot, f_i	0.80
Effective pulse energy per τ_i within 3 σ_{xy} focal spot	$E_i(\tau_i/\tau_{i\text{beam}})f_i = 0.75\,\mu$J
Effective number of inducing photons, N_i	4.0×10^{12} photons
Beam diameter of pulse, d_i	$(16.63 \pm 0.03 \pm 0.84)$ mm
Polarization	circular (left-handed state)
Focal length of off-axis parabolic mirror, f	279.1 mm
Single-photon detection efficiency, ϵ_{det}	1.4%
Efficiency of optical path from IP to PMT, ϵ_{opt}	33%
Total number of shots in S-pattern, W_{S}	15,000 shots
δn_{opt}	427.7

Table 2. Experimental parameters for numerical calculation of the exclusion limits in the $m - g/M$ parameter spaces.

evaluation of the upper limits on the coupling-mass relation, we numerically solve

$$2.24\delta n_{\text{opt}} = \mathcal{Y}_{c+i}(m, g/M; P)t_a r\epsilon, \tag{5.4}$$

where $t_a r = W_{\text{S}} = 15,000$, and the overall efficiency $\epsilon \equiv \epsilon_{\text{opt}}\epsilon_{\text{det}}$, with ϵ_{opt} being the optical path acceptance to the signal detector position and ϵ_{det} the single photon detection efficiency.

JHEP10(2022)176

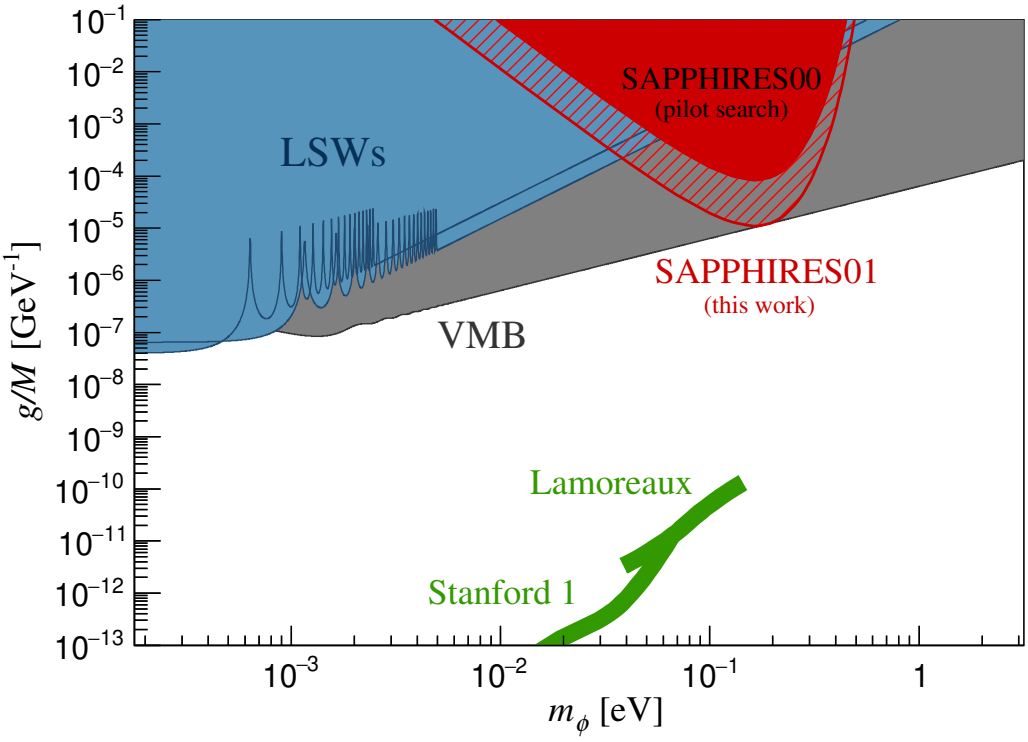

Figure 11. Upper limit in the $m_\phi - g/M$ parameter space for scalar field exchanges achieved in this work, SAPPHIRES01, represented by the red shaded area. The red filled area is from the pilot search, SAPPHIRES00 [11]. Limits from the LSW experiments (ALPS [7] and OSQAR [9]) and the VMB experiment (PVLAS [10]) are shown in the blue and gray areas, respectively. The green lines are exclusion limits from the non-Newtonian force searches (Stanford 1 [16]) and the Casimir force measurement (Lamoreaux [17]).

Figures 11 and 12 provide the evaluated upper limits of the coupling-mass relations for scalar and pseudoscalar fields, respectively, at a 95% confidence level. The red shaded areas are from this work, while the red filled areas are from previous searches [11].[2] The ALPS [7] and OSQAR [9] experiments are "Light Shining through Wall (LSW)" experiments and are filled with blue. The individual sinusoidal terms in the sensitivities from ALPS and OSQAR are simplified to 1 above 5.0 meV and 2.5 meV, respectively. The gray area is the region excluded by the vacuum magnetic birefringence (VMB) experiment (PVLAS [10]). In figure 11, the lines with green are excluded by a non-Newtonian force search (Stanford 1 [16]) and a Casimir force measurement (Lamoreaux [17]). In figure 12, the green area is the region excluded by a Helioscope experiment (CAST [18–21]). The yellow band is a region corresponding to the benchmark QCD axion model (KSVZ [22, 23]) with $0.07 < |E/N - 1.95| < 7$. The black dashed and solid lines are predicted by the KSVZ model with $E/N = 0$ and the DFSZ [24, 25] model with $E/N = 8/3$, respectively.

[2] As for figure 12, we note that the limit from the previous search [11] is rescaled due to the factor 1/2 in the new definition for the dual electromagnetic tensor in eq. (1.1).

JHEP10(2022)176

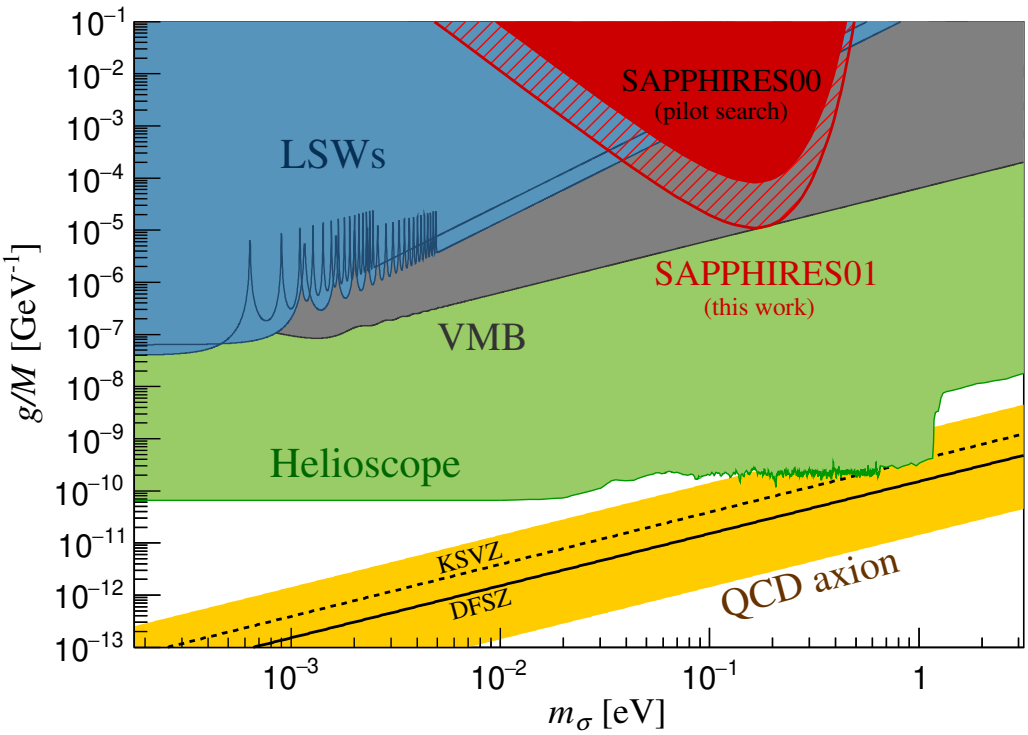

Figure 12. Upper limit in the $m_\sigma - g/M$ parameter space for pseudoscalar field exchanges achieved in this work, SAPPHIRES01, represented by the red shaded area. The red filled area is from the pilot search, SAPPHIRES00 [11]. Limits from the LSW experiments (ALPS [7] and OSQAR [9]), the VMB experiment (PVLAS [10]), and a Helioscope experiment (CAST [18–21]) are shown with the blue, gray, and green filled areas, respectively. The yellow band and the black dashed lines represent QCD axion predictions from the KSVZ model [22, 23] with $0.07 < |E/N - 1.95| < 7$ and $E/N = 0$, respectively. The solid line is the prediction from the DFSZ [24, 25] model with $E/N = 8/3$.

6 Conclusions

In this paper, we performed a stimulated resonant photon-photon collider experiment using two lasers with pulse energies around one order of magnitude higher than those in previous searches [11]. The generation of background photons via the atomic four-wave mixing (aFWM) process in optical elements was observed for the first time. By measuring the creation beam cross section dependence of the number of FWM photons, we observed a constant behavior, indicating that the observed photons originated only from the optical-element aFWM background. The expected value for the number of observed photons from resonant scattering via ALP exchanges was consistent with null. We then obtained the upper limit, which reached its maximum sensitivity in the coupling $g/M = 1.14 \times 10^{-5}\,\mathrm{GeV}^{-1}$ at $m = 0.18\,\mathrm{eV}$.

In this search the window material between the interaction chamber and the transport chamber was introduced to keep a high vacuum condition in the interaction chamber and to investigate how to handle optical-element aFWM background in real data analy-

JHEP10(2022)176

sis. We then succeeded in establishing the method for discussing ALP exchanges under a nonzero pressure-independent background, based on the beam cross-section dependence of the FWM yield. In future searches a specialized intermediate chamber without the window material will be inserted, which will reduce the optical-element background even if we increase the intensities of both beams. Building off of the established method, we expect the upgrade to higher laser intensities to drastically improve the sensitivity to ALP exchanges.

Acknowledgments

The T^6 system was financially supported by the MEXT Quantum Leap Flagship Program (JPMXS0118070187) and the program for advanced research equipment platforms (JPMXS0450300521). Y. Kirita acknowledges support from the JST, the establishment of university fellowships for the creation of science technology innovation, Grant No. JPMJFS2129, and a Grant-in-Aid for JSPS fellows No. 22J13756 from the Ministry of Education, Culture, Sports, Science and Technology (MEXT) of Japan. K. Homma acknowledges the support of the Collaborative Research Program of the Institute for Chemical Research at Kyoto University (Grant Nos. 2018–83, 2019–72, 2020–85, 2021–88, and 2022–101) and Grants-in-Aid for Scientific Research Nos. 17H02897, 18H04354, 19K21880, and 21H04474 from the Ministry of Education, Culture, Sports, Science and Technology (MEXT) of Japan. The authors in ELI-NP acknowledge the support from Extreme Light Infrastructure Nuclear Physics Phase II, a project co-financed by the Romanian Government and the European Union through the European Regional Development Fund and the Competitiveness Operational Programme (No. 1/07.07.2016, COP, ID 1334).

References

[1] R.D. Peccei and H.R. Quinn, *CP Conservation in the Presence of Pseudoparticles*, *Phys. Rev. Lett.* **38** (1977) 1440 [INSPIRE].

[2] R. Daido, F. Takahashi and W. Yin, *The ALP miracle revisited*, *JHEP* **02** (2018) 104 [arXiv:1710.11107] [INSPIRE].

[3] Y. Fujii and K. Maeda, *The Scalar-Tensor Theory of Gravitation*, Cambridge University Press (2003).

[4] Y. Fujii and K. Homma, *An approach toward the laboratory search for the scalar field as a candidate of Dark Energy*, *Prog. Theor. Phys.* **126** (2011) 531 [*Erratum ibid.* **2014** (2014) 089203] [arXiv:1006.1762] [INSPIRE].

[5] J. Khoury and A. Weltman, *Chameleon fields: Awaiting surprises for tests of gravity in space*, *Phys. Rev. Lett.* **93** (2004) 171104 [astro-ph/0309300] [INSPIRE].

[6] T. Katsuragawa, S. Matsuzaki and K. Homma, *Hunting dark energy with pressure-dependent photon-photon scattering*, *Phys. Rev. D* **106** (2022) 044011 [arXiv:2107.00478] [INSPIRE].

JHEP10(2022)176

[7] K. Ehret et al., *New ALPS Results on Hidden-Sector Lightweights*, *Phys. Lett. B* **689** (2010) 149 [arXiv:1004.1313] [INSPIRE].

[8] K. Homma, T. Hasebe and K. Kume, *The first search for sub-eV scalar fields via four-wave mixing at a quasi-parallel laser collider*, *Prog. Theor. Exp. Phys.* **2014** (2014) 083C01 [arXiv:1405.4133] [INSPIRE].

[9] OSQAR collaboration, *New exclusion limits on scalar and pseudoscalar axionlike particles from light shining through a wall*, *Phys. Rev. D* **92** (2015) 092002 [arXiv:1506.08082] [INSPIRE].

[10] A. Ejlli et al., *The PVLAS experiment: A 25 year effort to measure vacuum magnetic birefringence*, *Phys. Rept.* **871** (2020) 1 [arXiv:2005.12913] [INSPIRE].

[11] SAPPHIRES collaboration, *Search for sub-eV axion-like resonance states via stimulated quasi-parallel laser collisions with the parameterization including fully asymmetric collisional geometry*, *JHEP* **12** (2021) 108 [arXiv:2105.01224] [INSPIRE].

[12] T. Hasebe et al., *Search for sub-eV scalar and pseudoscalar resonances via four-wave mixing with a laser collider*, *Prog. Theor. Exp. Phys.* **2015** (2015) 073C01 [arXiv:1506.05581] [INSPIRE].

[13] A. Nobuhiro et al., *Extended search for sub-eV axion-like resonances via four-wave mixing with a quasi-parallel laser collider in a high-quality vacuum system*, *Prog. Theor. Exp. Phys.* **2020** (2020) 073C01 [arXiv:2004.10637] [INSPIRE].

[14] A. Yariv, *Optical Electronics in Modern Communications*, Oxford University Press (1997).

[15] K. Homma and Y. Kirita, *Stimulated radar collider for probing gravitationally weak coupling pseudo Nambu-Goldstone bosons*, *JHEP* **09** (2020) 095 [arXiv:1909.00983] [INSPIRE].

[16] J. Chiaverini, S.J. Smullin, A.A. Geraci, D.M. Weld and A. Kapitulnik, *New experimental constraints on non-Newtonian forces below* 100 *microns*, *Phys. Rev. Lett.* **90** (2003) 151101 [hep-ph/0209325] [INSPIRE].

[17] S.K. Lamoreaux, *Demonstration of the Casimir force in the* 0.6 *to* 6 *micrometers range*, *Phys. Rev. Lett.* **78** (1997) 5 [*Erratum ibid.* **81** (1998) 5475] [INSPIRE].

[18] CAST collaboration, *Probing eV-scale axions with CAST*, *JCAP* **02** (2009) 008 [arXiv:0810.4482] [INSPIRE].

[19] CAST collaboration, *Search for Sub-eV Mass Solar Axions by the CERN Axion Solar Telescope with* ^{3}*He Buffer Gas*, *Phys. Rev. Lett.* **107** (2011) 261302 [arXiv:1106.3919] [INSPIRE].

[20] CAST collaboration, *Search for Solar Axions by the CERN Axion Solar Telescope with* ^{3}*He Buffer Gas: Closing the Hot Dark Matter Gap*, *Phys. Rev. Lett.* **112** (2014) 091302 [arXiv:1307.1985] [INSPIRE].

[21] CAST collaboration, *New CAST Limit on the Axion-Photon Interaction*, *Nature Phys.* **13** (2017) 584 [arXiv:1705.02290] [INSPIRE].

[22] J.E. Kim, *Weak-Interaction Singlet and Strong CP Invariance*, *Phys. Rev. Lett.* **43** (1979) 103 [INSPIRE].

[23] M.A. Shifman, A.I. Vainshtein and V.I. Zakharov, *Can Confinement Ensure Natural CP Invariance of Strong Interactions?*, *Nucl. Phys. B* **166** (1980) 493 [INSPIRE].

JHEP10(2022)176

[24] M. Dine, W. Fischler and M. Srednicki, *A Simple Solution to the Strong CP Problem with a Harmless Axion*, *Phys. Lett. B* **104** (1981) 199 [INSPIRE].

[25] A.R. Zhitnitsky, *On Possible Suppression of the Axion Hadron Interactions* (in Russian), *Sov. J. Nucl. Phys.* **31** (1980) 260 [*Yad. Fiz.* **31** (1980) 497] [INSPIRE].

[26] PARTICLE DATA collaboration, *Review of Particle Physics (RPP)*, *Phys. Rev. D* **86** (2012) 010001 [INSPIRE].

JHEP10(2022)176